Autonomous Airdrop Systems Employing Ground Wind Measurements for Improved Landing Accuracy

Martin R. Cacan, Edward Scheuermann, Michael Ward, Mark Costello, and Nathan Slegers

***Abstract*—Aerial cargo delivery, also known as airdrop, systems are heavily affected by atmospheric wind conditions. Guided airdrop systems typically employ onboard wind velocity estimation methods to predict the wind in real time as the systems descend, but these methods provide no foresight of the winds near the ground. Unexpected ground winds can result in large errors in landing location, and they can even lead to damage or complete loss of the cargo if the system impacts the ground while traveling downwind. This paper reports on a ground-based mechatronic system consisting of a cup and vane anemometer coupled to a guided airdrop system through a wireless transceiver. The guidance logic running on the airdrop system's onboard autopilot is modified to integrate the anemometer measurements at ground level near the intended landing zone with onboard wind estimates to provide an improved, real-time estimate of the wind profile. The concept was first developed in the framework of a rigorous simulation model and then validated in the flight test. Both simulation and subsequent flight tests with the prototype system demonstrate reductions in the landing position error by more than 30% as well as a complete elimination of potentially dangerous downwind landings.**

***Index Terms*—Anemometer, autonomous, guided airdrop, landing accuracy, parafoil, payload, wind estimation, wind profile.**

I. Introduction

AIRDROP systems have been used for decades in military and humanitarian aid operations to deliver supplies quickly to hard to reach locations. Characteristically employed in the field due to their low cost, unguided system landing accuracy is highly dependent on accurate release timing from the aircraft and wind drift during descent [1]–[3]. Guided airdrop systems typically employ ram-air parafoils which have the ability to penetrate the atmospheric winds and steer using trailing edge brake deflection. The basic flight profile of guided airdrop systems is shown in Fig. 1. After the system is released, it loiters upwind of the target in order to prevent getting trapped downwind. During final approach to the target, the guided airdrop system lines up for landing facing into the wind in order to reduce ground speed and minimize the impact energy at landing to maximize payload survivability. Guided systems offer much greater flexibility over unguided systems as they can be dropped with a significant offset from the drop zone. Their implementation in the field to date has been limited due to increased costs associated with upgrading to "smart" systems. As such, focusing on low-cost improvements is essential for the guided airdrop system to achieve increased field deployment.

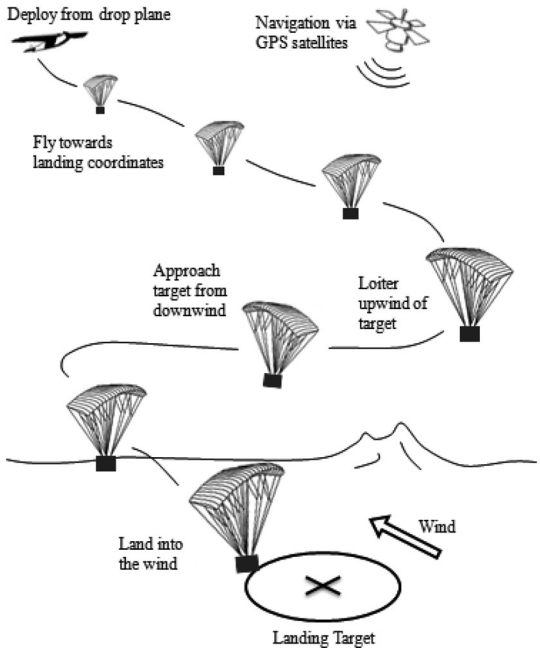

Fig. 1. Typical flight profile for modern guided airdrop.

Inaccurate information regarding the atmospheric wind velocity field around the drop zone is the most significant source of error in landing accuracy for guided airdrop systems [4]–[6]. Additionally, guided airdrop systems utilizing parafoils fly with a significant horizontal velocity component, and it is critical that these systems land facing into the wind to minimize the impact speed. Large errors in the estimates of the ground wind direction can lead to crosswind or downwind landings at high speed, resulting in destruction of the payload. Wind velocity estimation techniques using data gathered exclusively from onboard sensors are powerful as they do not require any other systems to be deployed, but provide only a lagged estimate of the wind [7]. Winds at lower altitudes remain unknown and can only be accounted for when flown through. To overcome this shortcoming, systems such as dropsondes [5], [8] or Doppler-based LIDAR

Manuscript received May 29, 2014; revised October 7, 2014; accepted December 23, 2014. Recommended by Technical Editor G. Herrmann. This work was supported by the U.S. Army Natick Soldier Systems Center, Natick, MA, USA.

M. R. Cacan and E. Scheuermann are with the Woodruff School of Mechanical Engineering, Georgia Institute of Technology, Atlanta, GA 30312, USA (e-mail: martincacan@gatech.edu; escheu2@gatech.edu).

M. Ward is with the Guggenheim School of Aerospace Engineering, Georgia Institute of Technology, Atlanta, GA 30312, USA (e-mail: mike.ward@gatech.edu).

M. Costello is with the Guggenheim School of Aerospace Engineering and Woodruff School of Mechanical Engineering, Georgia Institute of Technology, Atlanta, GA 30312, USA (e-mail: mark.costello@aerospace.gatech.edu).

N. Slegers is with the College of Engineering, George Fox University, Newberg, OR 97132, USA (e-mail: nslegers@georgefox.edu).

Color versions of one or more of the figures in this paper are available online at http://ieeexplore.ieee.org.

Digital Object Identifier 10.1109/TMECH.2015.2405851

units [9], [10] are used to estimate the wind velocity at a variety of altitudes creating detailed wind velocity profile maps. Utilizing LIDAR systems for atmospheric wind velocity mapping yields highly improved landing accuracy [9], but is also expensive and difficult to deploy in remote areas due to the significant size and power requirements of the LIDAR unit itself.

In many airdrop applications, a trained crew is waiting on the ground to receive the cargo. In these scenarios, the ground crew could be provided with a device capable of measuring the ground winds and broadcasting this data up to the incoming airdrop systems as long as the device is kept simple, compact, and lightweight. The work reported here employs a simple, inexpensive cup and vane anemometer coupled to a wireless transceiver capable of communicating the anemometer measurements to the guided airdrop system in real time. The autonomous guidance logic running onboard the airdrop system was modified to integrate the anemometer measurements at the ground level, near the intended landing zone, with onboard wind estimates to provide an improved real-time estimate of the wind profile. The goal of the current study is to quantify the benefits of this type of device in terms of landing accuracy and the ability to land into the wind, which can be viewed as a surrogate measure of landing survivability. Details regarding the necessary changes to conventional airdrop system autonomous control logic in order to incorporate ground wind measurements are presented in Section II. Section III explores the landing accuracy improvements from the inclusion of a ground wind anemometer through simulation of a validated computer model. Simulation results are validated in Section IV through experimental flight testing of a small-scale parafoil and payload system. This is followed by the conclusions and findings of this paper.

II. Guidance, Navigation, and Control

The onboard computer executes the guidance, navigation, and control (GNC) algorithm which is used to perform path planning, estimate relevant state and atmospheric conditions, and track the desired path using parafoil control inputs. Details on the calculations are provided below including a discussion on how ground wind estimates from the cup anemometer are integrated into these calculations. It is important to note the control logic used for this study represents common practice in the airdrop community, with the exception of the additional logic which incorporates ground wind velocity information used to plan final approach.

A. Guidance Algorithm

The guidance algorithm has inputs from measured and estimated state and atmospheric conditions, and executes path planning to accurately reach the landing target. Instead of attempting path planning in the presence of atmospheric winds, a wind-based reference frame (WF) is established which is associated with the drift expected from the influence of the atmospheric winds. Utilizing the WF is advantageous as it decouples the absolute system movement into no wind flight conditions and the drift caused by atmospheric winds. This wind-based frame is a moving reference frame. At ground level, the origin of this frame is pinned to the target. Propagating upward, the origin is shifted horizontally to account for the drift associated with the assumed wind profile. The wind frame is oriented with the $\hat{i}_{\mathrm{WF}}$-axis aligned with the wind direction expected at the ground level. A diagram outlining the change in reference frames is presented in Fig. 2. This method was initially introduced by Goodrick and Murphy [11], and more recently by Jann [12], who shifted the reference frame horizontally, $(\Delta x, \Delta y)$, based upon the integral of the wind profile and descent rate from ground level to the payload altitude *h*

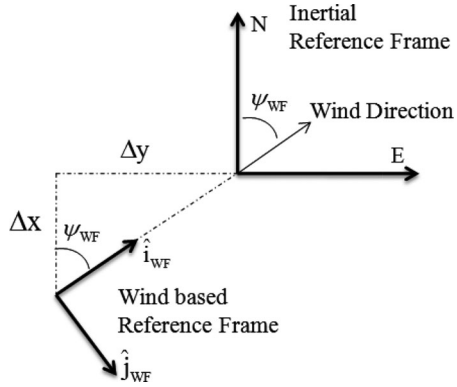

Fig. 2. Visual representation of the WF. It is offset from the inertial origin by an amount $(\Delta x, \Delta y)$ and rotated to align with the ground wind direction.

$$\Delta x = \int_0^h \frac{V_{Wx}(z)}{\dot{z}(z)} dz$$
$$\Delta y = \int_0^h \frac{V_{Wy}(z)}{\dot{z}(z)} dz. \quad (1)$$

Here, $V_{Wx}(z)$ and $V_{Wy}(z)$ are the horizontal wind velocity components in the inertial frame and $\dot{z}(z)$is the vertical velocity component of the aircraft in the inertial frame. The formula in (1) can be simplified by assuming a constant descent rate for the system which is normally an excellent assumption for airdrop systems [13], [14]. Using an estimate of the wind profile, a set of altitude-averaged wind components $(\tilde{V}_{Wx}, \tilde{V}_{Wy})$ are defined which represent the bulk average of the wind profile from the current altitude to the ground

$$\tilde{V}_{Wx} = \frac{1}{h}\int_0^h V_{Wx}(z)\, dz$$
$$\tilde{V}_{Wy} = \frac{1}{h}\int_0^h V_{Wy}(z)\, dz. \quad (2)$$

The position of the parafoil and payload system in the WF is defined based on the inertial position and expected wind drift

$$x_{WF} = x_I + \frac{h}{\dot{z}}\tilde{V}_{Wx}$$
$$y_{WF} = y_I + \frac{h}{\dot{z}}\tilde{V}_{Wy}. \quad (3)$$

It is important to note that vertical atmospheric winds are not used to shift the WF as thermals and local sinks have a high amount of spatial variability and often do not persist throughout the entire flight. The orientation of the WF is rotated using the measurements from the ground wind anemometer,

V_{Wx}^G and V_{Wy}^G, to align the $\hat{i}_{WF}$-axis with the ground wind direction

$$\psi_{WF} = \mathrm{a\,tan}\left(\frac{V_{Wy}^G}{V_{Wx}^G}\right). \tag{4}$$

The primary benefit of the work discussed in this paper arises from the inclusion of ground anemometer measurements to the assumed wind profile. With the combination of onboard atmospheric wind estimates and ground anemometer wind measurements, the wind field is assumed linear across the altitude between these two points. The linear wind model was chosen as a reasonable estimate of an instantaneous wind field and is standard practice in guided airdrop applications [13], [15]. Furthermore, the utilization of other assumed wind profiles, such as an exponential variation [16], [17] were found to have only a minor effect on the overall landing accuracy. The methodology presented here is not specific to the shape of the assumed wind profile. The key point and the primary source of improved landing accuracy and landing survivability is that the assumed wind profile is seeded with a real-time measurement of the actual ground wind magnitude and direction.

During flight, the guidance algorithm defines waypoints in the WF for the control algorithm to track. A waypoint is defined as a commanded point in space with an associated heading requirement. The guidance algorithm generates a path from the current position and heading angle to the desired position and heading angle at the next waypoint. Dubins path planning is used and works to minimize the flight distance with three maneuver elements: initially turning at a constant rate in the direction of the next waypoint, flying straight to approach the waypoint, and when near the waypoint, turning to match desired heading defined by the waypoint [12], [13], [18].

The guidance algorithm is decomposed into 4 stages (initialization, loiter, approach, and flare) which enable accurate landing.

1) Initialization Phase: During this phase, initial estimates for the airspeed of the parafoil and payload system, and horizontal wind components are computed. This provides an initial condition for the navigation algorithm which will continue to estimate these quantities after the initialization period. At the onset of the initialization phase, the parafoil and payload system turns with a constant differential brake deflection resulting in a near circular flight path. Over this period, airspeed and atmospheric winds are assumed constant. The resulting ground velocity profile during this period is sinusoidal in nature as the aerial vehicle velocity vector combines both constructively and destructively with the atmospheric wind velocity depending on the heading. The atmospheric wind components, V_{Wx} and V_{Wy}, can be identified by solving the following equation:

$$\begin{bmatrix} \dot{x}_1^{gps} - \mu_{\dot{x}} & \dot{y}_1^{gps} - \mu_{\dot{y}} \\ \vdots & \vdots \\ \dot{x}_N^{gps} - \mu_{\dot{x}} & \dot{y}_N^{gps} - \mu_{\dot{y}} \end{bmatrix} \begin{Bmatrix} V_{Wx} \\ V_{Wy} \end{Bmatrix} = \frac{1}{2} \begin{bmatrix} \left(V_1^2\right)^{gps} - \mu_{V^2} \\ \vdots \\ \left(V_N^2\right)^{gps} - \mu_{V^2} \end{bmatrix}. \tag{5}$$

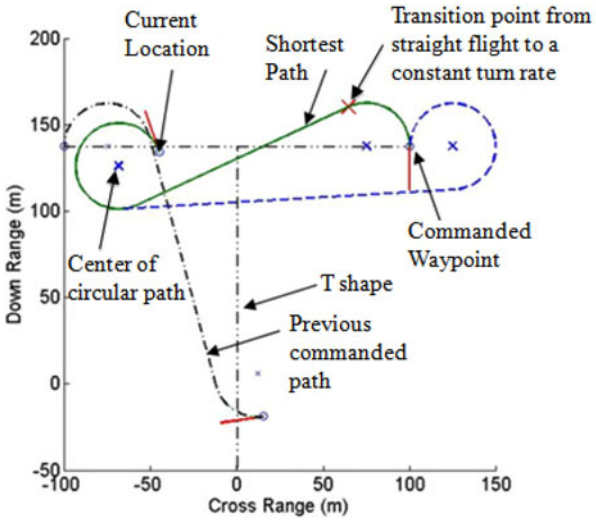

Fig. 3. Visualization of Dubins path planning transitioning from the left waypoint to the right.

Here, $\dot{x}_i^{gps}$ and $\dot{y}_i^{gps}$ indicate measured GPS velocity components, and $\left(V_i^2\right)^{gps}$ is the squared velocity magnitude. μ_A is the average value of parameter A in the set of data and N is the number of data points collected in the initialization period. Finally, the airspeed of the parafoil and payload system V_0 can be estimated using the measured GPS data and horizontal wind estimates:

$$V_{0,i} = \sqrt{\left(\dot{x}_i^{gps} - V_{Wx}\right)^2 + \left(\dot{y}_i^{gps} - V_{Wy}\right)^2}, \quad V_0 = \mu_{V_0}. \tag{6}$$

Furthermore, details on (5) and (6) are provided in [7].

2) Loiter Phase: After the initialization phase, the system can define the WF, or a frame that accounts for the drift of the aircraft due to the wind. This is constantly updated as the wind changes as a function of space and time. During this phase, the parafoil and payload system flies through a set of figure eight turns in order to maintain position relative to the target. This method, suggested by Jann [12], is implemented by assigning homing targets at specified distance downwind and specified distance perpendicular to a line drawn straight downwind from the target. These reference lines form the *T* approach utilized by this system and are shown as black- dashed lines in Fig. 3. When commanding figure eight turns, the system always turns upwind when reaching waypoints preventing large drifts downwind.

Fig. 3 illustrates the path planning during transition from initialization to figure eight turns. The key is to study the geometry of the situation by analyzing Dubins path options with circles of the set radius (one at the starting location and one at the end) and the straight line that is tangent to both circles. The algorithm analyzes four paths the system could take, turning left or right from the current location and approaching the final location turning either left or right (Fig. 3 only shows two of these options). The shortest total distance is the path chosen by the guidance algorithm, denoted by the solid line in Fig. 3. Note, one of the three suboptimal paths is also shown as the dashed line.

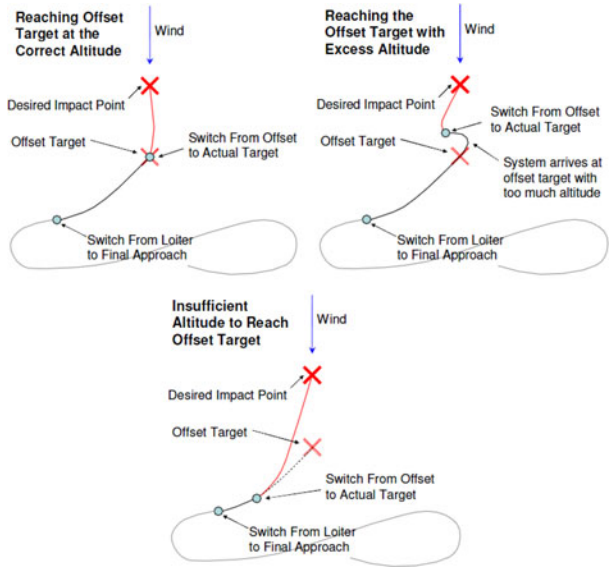

Fig. 4. Cases outlining two-stage final approach methodologies [19].

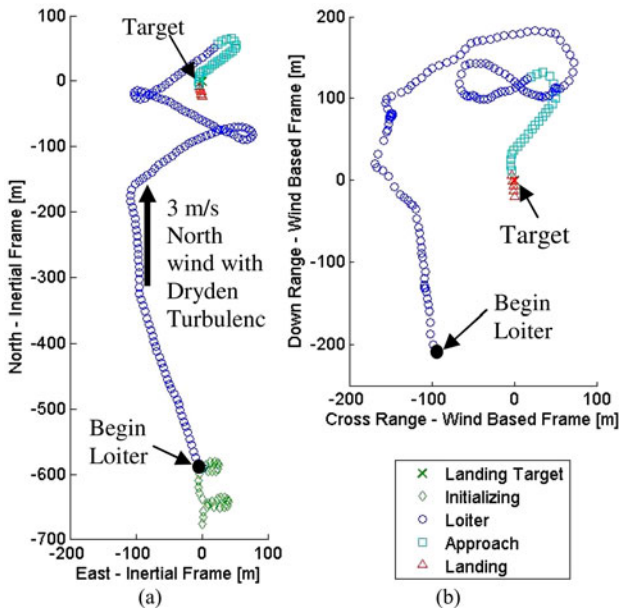

Fig. 5. Sample simulated flight trajectory of the guided airdrop system in (a) inertial frame and (b) wind-based frame.

In Fig. 3, the parafoil and payload system has reached the first waypoint (defined by a circular space around the waypoint) and switches to track the next waypoint. The new path chosen by the autopilot does not take it directly through the previous waypoint as precisely reaching it is not necessary, only reaching a given proximity. This flexibility is removed when tracking the final landing point to ensure accurate landings.

During the entire loitering period, the altitude required to reach the target from the current location is computed constantly. The instantaneous distance to the target is defined by the arc of the circle required to turn from the current heading to point at the target, and the straight line between the end of this turning circle and the target

$$L = |d\psi|\, R + \|\bar{x}_1 - \bar{x}_T\|\,. \tag{7}$$

Here, $d\psi, R, \bar{x}_1,$ and $\bar{x}_T$ are the change in heading, turning radius, the coordinates at the end of the turn, and the coordinates of the landing target. This is then converted into the required height based on the estimated descent rate and airspeed

$$h_{\mathrm{REQ}} = L\frac{\dot{z}}{V_0}. \tag{8}$$

When the current altitude drops below h_{REQ}, the system switches into the approach phase.

3) Approach Phase: This section deviates from the figure eight holding pattern and attempts to fly along the stem of the T upwind toward the target. An offset target is introduced that is downwind of the desired impact point which ensures that the end of the trajectory is a straight line segment pointed into the wind. Some adjustments can be made to the trajectory if the system is going to reach the offset target with too much or too little altitude. If the system has too much altitude, the system flies a portion of a circle until the excess altitude is lost and the current height equals the height required to reach the landing point. If the system has too little altitude, the offset target is abandoned early, and the system flies directly to the landing point. These three cases are demonstrated in Fig. 4.

4) Flare Phase: The goal of the landing maneuver is to minimize the kinetic energy of the system just before the impact. Below a preset altitude threshold, the system is commanded to fly upwind, even if it means turning away from the target. Just before the impact, full symmetric brake is then applied to flare the canopy just short of stall in order to slow the airspeed of the airdrop system.

An example flight history is shown in Fig. 5 to highlight all four stages of the guidance algorithm. The simulation was initialized with the airdrop system located approximately 700 m upwind of the target in the inertial reference frame. On the left, the simulation results are plotted in the inertial frame, as such, the previously discussed T-shape approach is continuously shifting to keep a constant offset distance in the WF. On the right, the simulation results are plotted in the WF, showing the fixed T-shape approach before landing into the wind, just past the target.

B. Navigation Algorithm

After the initialization phase where initial estimates of the atmospheric wind velocities and assumed constant airspeed are found, two Kalman filters are used to update estimates and filter measurement noise. The GPS sensor provides measured location and velocities in the inertial reference frame. A conventional, stationary linear Kalman filter estimates position and velocity in order to reject the sensor noise [20].

An extended Kalman filter is used to estimate the components of the horizontal wind, vehicle heading, and vehicle heading rate. This filter varies from the stationary case in that the Kalman

filter gain, G_{KF}, is calculated in real time and depends on the current heading angle and velocity

$$\begin{bmatrix} W_{x,i+1}^{nv} \\ W_{y,i+1}^{nv} \\ \psi_{i+1}^{nv} \\ \dot{\psi}_{i+1}^{nv} \end{bmatrix} = \begin{bmatrix} W_{x,i}^{nv} \\ W_{y,i}^{nv} \\ \psi_{i}^{nv} + dt\dot{\psi}_{i}^{nv} \\ \dot{\psi}_{i}^{nv} \end{bmatrix} + G_{\mathrm{KF}} \left(\begin{bmatrix} \dot{x}_{i+1}^{gps} \\ \dot{y}_{i+1}^{gps} \end{bmatrix} - \begin{bmatrix} W_{x,i}^{nv} + V_0 \cos\left(\psi_i^{nv}\right) \\ W_{y,i}^{nv} + V_0 \sin\left(\psi_i^{nv}\right) \end{bmatrix} \right). \quad (9)$$

More details on the navigation algorithm can be found in [19]. As the guidance computer now has an accurate estimate of system parameters, it can work to control certain states to land accurately at the target.

C. Control Algorithm

The airdrop system is controlled using left and right trailing edge brake deflection. This increases drag on a specific side of the canopy, inducing lateral turning control allowing the guidance algorithm to track a commanded heading angle. The steering is done through a PI controller. The proportional component is nonlinear to reduce the control effort when the heading error is small. Based on the current waypoint target supplied by the guidance algorithm and the estimated location of the system in the WF, a commanded heading value is generated. This is compared to the actual heading filtered by the navigation algorithm and mapped to a commanded turn rate, TR_c

$$\Delta\psi = \psi_c - \psi^{nv} \quad (10)$$

$$\Delta\psi_{\mathrm{ratio}} = \frac{\Delta\psi}{\Delta\psi_{\max}} \quad (11)$$

$$\mathrm{TR}_c = \begin{cases} \mathrm{TR}_{\max}, \Delta\psi_{\mathrm{ratio}} \geq 1 \\ -\mathrm{TR}_{\max}, \Delta\psi_{\mathrm{ratio}} \leq -1 \\ \mathrm{TR}_{\max}\Delta\psi_{\mathrm{ratio}}\sqrt{|\Delta\psi_{\mathrm{ratio}}|}, \quad \text{else} \end{cases}. \quad (12)$$

From the desired turn rate, asymmetric brake deflection, δa_c, is determined based on an actuator gain and bias term. The gain is a design parameter set to match the expected turn rate response of the vehicle, and the asymmetric brake bias is computed from the integral control logic allowing the system to fly straight under no control

$$\delta a_c = G_{\delta a}\mathrm{TR}_c + \delta a_{\mathrm{bias}}. \quad (13)$$

It should be noted that δa_c is a parameter that varies in the span $[-1, 1]$ signifying the maximum turning effort in both left and right directions. This asymmetric brake parameter is then converted into the individual brake deflection of the left and right trailing edge, δl_c and δr_c, respectively,

$$\delta l_c = \delta b_c - \frac{1}{2}\delta a_c$$

$$\delta r_c = \delta b_c + \frac{1}{2}\delta a_c. \quad (14)$$

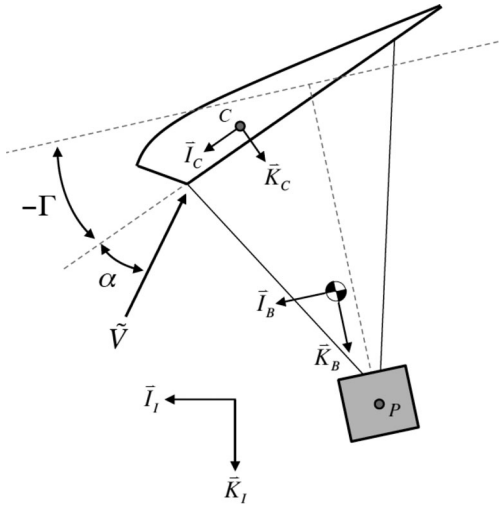

Fig. 6. Parafoil and payload schematic.

Here, the symmetric brake level δb_c is included in order to command a flare. To achieve a desired turn rate, each actuator only needs to act over half of the needed brake differential, leading to faster actuator response. Also, this method tends to have a lesser impact on the nominal airspeed of the airdrop system during turning, making path planning computationally more efficient. Only under flare in the final stage of the guidance algorithm, does the symmetric brake level change in order to slow the system to near stall prior to landing. Additionally note that based on these definitions, δl_c and $\delta \mathrm{r}_c$are mapped from 0 to 1 which is the minimum to maximum range of the brake actuators.

III. Simulation Results

A. Parafoil and Payload Model

Fig. 6 shows a schematic of a parafoil and payload system. With the exception of movable trailing edge brakes, the parafoil canopy is considered to be a fixed shape. The combined system of the parafoil canopy and the payload are represented by six degrees of freedom, rigid-body model, defined by three inertial position components of the total system mass center as well as the three Euler orientation angles. The canopy aerodynamic forces and moments are computed about the canopy aerodynamic center (see point C in Fig. 6). The transformation from the body frame (see frame *B* in Fig. 6) to the canopy reference frame (see frame *C* in Fig. 6) is defined by a single-axis rotation in pitch by the canopy incidence angle Γ. The equations of motion for this six degree of freedom parafoil and payload representation have been derived previously and validated through flight testing [6], [7], [19].

B. Simple Wind Shear Model

To capture atmospheric wind conditions typically observed at low altitudes, a simple wind shear model was created. Low-frequency, large-scale components of the wind are generated by a horizontal wind profile which is variable between flights and

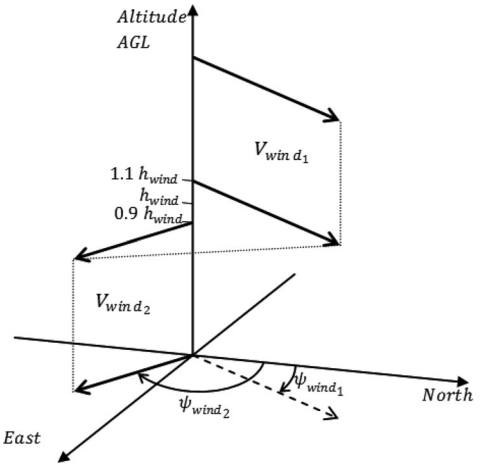

Fig. 7. Horizontal wind shear profile [9].

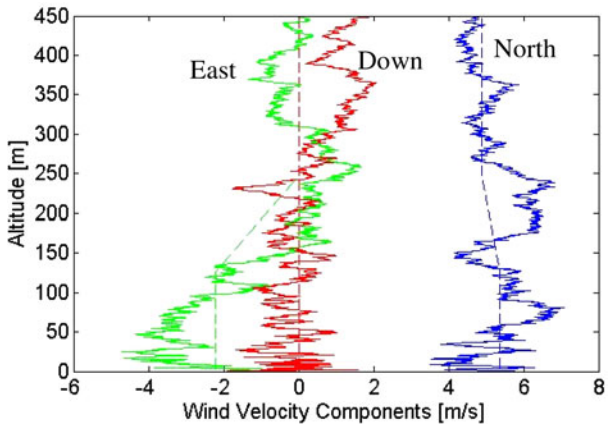

Fig. 8. Example wind profile showing underlying simple shear model (dashed lines) and complete model with superimposed Dryden turbulence (solid lines).

constant during a particular flight. This wind field, presented in Fig. 7, is meant to capture large-scale, slowly varying features such as wind shear. In a simple and concise manner, this wind model captures the nature of atmospheric wind fields close to the ground. By statistically varying the parameters that comprise the model, a rich variety of physical scenarios can be constructed.

To capture high-frequency, small-scale components of the wind, turbulence is generated according to the Dryden turbulence spectrum. Gust velocities and angular rate components are computed for all three axes by driving discrete filters with unit-variance and independent white noise signals [21]. A sample wind field created by the simple shear model with and without Dryden turbulence is shown in Fig. 8.

This common atmospheric model, though simple in form, varies significantly from the conventionally assumed altitude-independent wind profile used to position the WF. The ability to use ground wind measurements to create a linearly varying wind profile has the ability to identify wind shears, though not the altitude at which it occurs. The ground anemometer provides the system with foresight to overcome altitude-dependent variations in the wind field.

Fig. 9. Small-scale parafoil and payload system during gliding flight.

TABLE I
MASS AND GEOMETRY PARAMETERS FOR THE EXPERIMENTAL PARAFOIL AND PAYLOAD SYSTEM

Parameter	Value	Units
Total Mass	2.87	kg
Span (b)	1.88	m
Chord (c)	0.8	m
Wing Area	1.5	m^2
Wing Loading	1.9	kg/m^2
Airspeed	7.2	m/s

C. Results

The parafoil and payload model presented previously is applied to a physical system used for experimental testing. The flight test system is presented in Fig. 9 with key geometry and weight characteristics of the test system given in Table I. Additional model parameters were matched to the physical system through system identification techniques [6], [7]. The ground anemometer shown in Fig. 10 was modeled to provide atmospheric ground wind feedback 4 m above ground level at the location of the target. With all simulation parameters identified to match experimental devices, system trajectories are integrated forward in time using a fourth-order Runge–Kutta fixed time step method.

An initial simulation is conducted that exemplifies the guidance logic variations between the conventional method and the improved method using a ground anemometer. The atmospheric conditions consist of the simple wind shear model where winds at an altitude flow north at 4 m/s while winds below 80 m, the wind shear altitude, blow southeast at 1.5 m/s. While this wind profile is realistic, it is slightly extreme in the shear conditions. It was chosen as an exemplary case to clearly highlight variation between the two cases considered.

Two trajectories are presented in Fig. 11, one using only onboard wind velocity estimates (nominal autonomous) and the other aided by ground wind measurements (anemometer aided). The clear variation between the two systems indicates that the ground anemometer is able to aid the airdrop system by providing prior knowledge of the ground wind direction. With only

Fig. 10. Anemometer mounted at the top of a tripod for atmospheric ground wind measurements. Visible in the background is an airdrop system lining up to land into the wind.

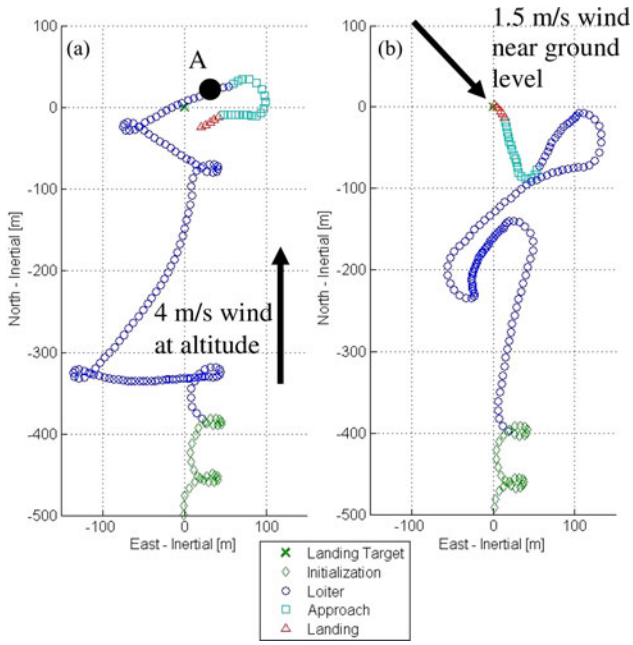

Fig. 11. Comparative simulated flight trajectories showing (a) nominal autonomous system and (b) anemometer-aided system.

onboard wind estimation, the airdrop system is unaware of the wind shear until it physically reaches it, near point A in Fig. 11. At this point, the WF rotates and shifts with updated wind predictions but lags the actual wind field due to inherent ability of the extended Kalman filter to update. Due to this behavior, the system lands into the direction of the expected wind direction, but lands at an almost 90° angle from the desired direction.

The airdrop system aided by anemometer ground wind measurements always knows the ground wind direction and can account for the wind shear. This is visible when comparing Fig. 11(a) and (b). The anemometer-aided system always stays downwind (southeast) of the target with respect to the ground winds as it has foreknowledge of the desired landing direction. The nominal autonomous system on the other hand attempts to place itself downwind of the target with respect to the onboard estimate. Due to the lagged nature of the estimation method, this is dominated by the northward high-altitude wind, and only when the system flies through the shear does it attempt to reorient and approach from the southeast.

To demonstrate statistically significant results, a set of Monte Carlo simulations were conducted to analyze the benefit of ground wind measurements. The landing accuracy of airdrop systems is typically reported in terms of the circular error probable (CEP). The 50% CEP is the radius of a circle centered about the target that contains 50% of the landing points. This is also referred to as the median miss distance. The 90% CEP is also studied as it has a better indication of outliers in the dataset and

TABLE II
WIND PROFILE PARAMETERS USED IN MONTE CARLO SIMULATION

Model Parameter	Variation Range
High Altitude Wind Speed	0–6 m/s
Low Altitude Wind Speed	0–6 m/s
High Altitude Wind Heading	0°
Low Altitude Wind Heading	0–360°
Height of Wind Shear	50–200 m
Release Altitude	450 m
Vertical RMS Dryden Intensity	0.1 – 0.7 m/s

follows a similar definition. For the simulations, Table II shows the range of wind field parameters used to model both calm and gusty conditions that align with conditions experienced during experimental testing.

Three cases were considered and 1000 complete flights were simulated for each case. First, the nominal autonomous control logic which uses only onboard estimates was tested yielding a benchmark case representing the current state of the art in guided airdrop systems. Second, simulated ground wind measurements were provided for incorporation into the guidance calculations. Third, a case was simulated where the true, mean horizontal wind profile was provided at 50-m altitude increments from 0 to 450 m. This last case represents the maximum improvement in landing accuracy that could be expected from the incorporation of any source of external knowledge of the horizontal wind profile into the onboard guidance calculations.

All of the simulated landing points for each of the three cases are shown in Fig. 12, and statistical values are presented in Table III. Landing points are plotted in the WF, where the ground wind flows from the bottom of the plot to the top, and the airdrop system should ideally approach the target from the top of the plot to land into the wind.

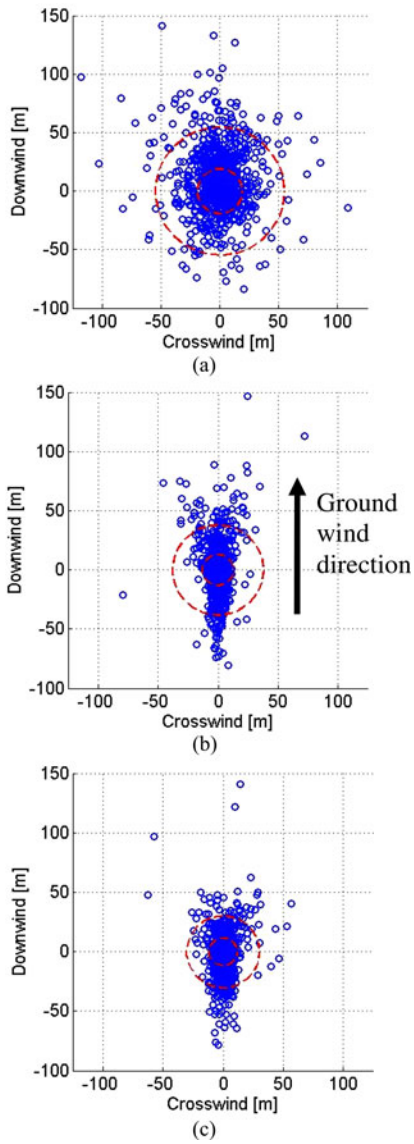

Fig. 12. Monte Carlo simulation results for (a) nominal autonomous system, (b) anemometer-aided system, and (c) system-provided full, mean horizontal wind profile. The inner and outer circles represent the 50% and 90% CEP values, respectively.

TABLE III
LANDING STATISTICS FROM MONTE CARLO SIMULATION RESULTS

Autonomous System	50% CEP	90% CEP	Reduction in 50% CEP
Nominal Autonomous	19.3 m	55.0 m	–
Anemometer Aided	13.2 m	38.3 m	32%
True Wind	11.8 m	30.4 m	39%

The nominal autonomous landing dispersion shows a relatively even distribution of points centered around the intended target. Several points indicate significant downwind and crosswind direction misses. Calculated 50% and 90% CEP values for the nominal autonomous system are 19.3 and 55.0 m, respectively. With the addition of a ground wind anemometer, CEP

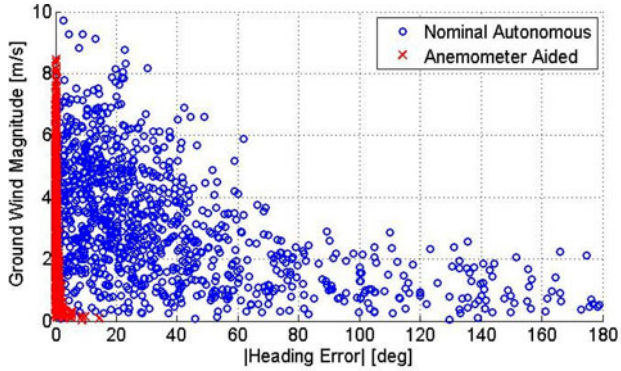

Fig. 13. Ability of the simulated nominal autonomous system and the anemometer-aided system to land into the wind.

values decrease to 13.2 m for 50% and 28.3 m for 90% CEP. Notable from the landing dispersion is the significant reduction in crosswind misses as the system has a far more accurate estimate of the ground wind direction. Misses are still prominent along the downwind axis. These are primarily attributed to the two remaining sources of uncertainty in the wind profile, being the vertical wind component, and the variation of the wind in time. The effects of these uncertainties could be mitigated with the use of longitudinal control to further improve landing accuracy [19], [22]. Finally, in the case where the guidance computer has a full horizontal wind profile map, the 50% CEP value decreases further to 11.8 m and the 90% CEP becomes 30.4 m.

It is fascinating to note that the addition of a single measurement of the ground wind to the guidance calculations achieves 80% of the improvement in landing accuracy expected from perfect knowledge of the entire wind profile. This indicates that by far the most critical piece of knowledge about the wind profile that can be provided to a guided airdrop system is a measurement of the wind at the ground.

Another primary benefit of knowledge of the ground wind is an improvement in the ability of the system to land facing into the wind. Fig. 13 shows the absolute value of the heading error, defined as the difference between the final heading angle of the airdrop system and the ideal heading-angle-pointed straight upwind, plotted against the ground wind magnitude. When the system is aided by the ground anemometer, the error is extremely small, never exceeding 10°. The nominal autonomous system shows significantly more error. On average, the nominal autonomous system had a landing heading error of 38°, with some errors as high as 180°, indicating a landing directly downwind.

IV. EXPERIMENTAL RESULTS

Simulation results were verified experimentally using the payload and parafoil system shown in Fig. 9. This system is equipped with an autopilot, servo motors, electric brushless motor, speed controller, and battery. The autopilot runs a PIC32MX family microcontroller and has a GPS receiver, barometric altimeter, and XBee wireless transceiver.

The GNC algorithm utilizes horizontal position and velocity estimates from the GPS receiver along with altitude and descent

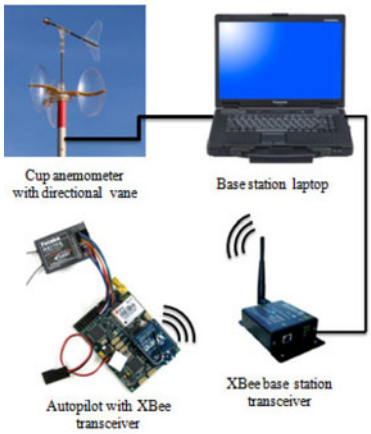

Fig. 14. Anemometer system used to provide ground wind measurements to the onboard autopilot.

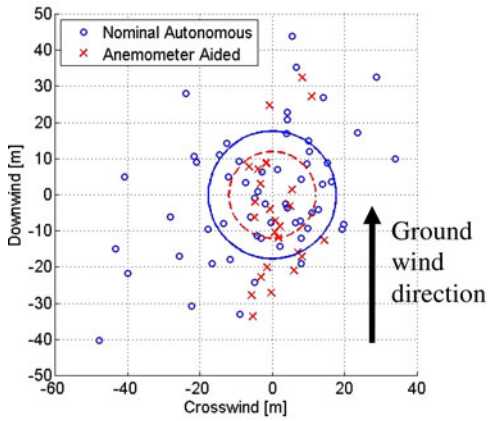

Fig. 15. Landing dispersion from flight tests of the nominal autonomous and anemometer-aided guided airdrop systems plotted in the WF. 50% CEP circles are presented for the nominal autonomous system (blue solid line) and anemometer-aided (dashed red line) cases.

rate estimates from the barometric altimeter to update system state estimates, wind estimates, trajectory calculations, and actuator commands at a rate of 4 Hz. The wireless transceiver is used to send GNC parameters to a ground base station at 1 Hz in order to monitor the parafoil and payload system during experimental flight. Additionally, all flight data are stored onboard in EEPROM memory for post processing and analysis.

Actuator commands generated from the control algorithm are sent to two high-torque servos which deflect the trailing edge of the canopy by reeling in rigging lines. Power is provided to the payload from a three-cell 6000-mAh battery, and delivers three-phase power to the brushless motor through the electronic speed controller. The rear-mounted motor and propeller are included to facilitate experimental testing using a "simulated drop" method. For this, the system is hand launched from ground level, flown under power to gain altitude until a desired "release" altitude is reached at which time the motor is turned OFF and the control logic is engaged for guided descent and landing. Based on the battery, motor, and propeller specifications, the vehicle can climb under power at approximately 120 m/min and conduct two flights per battery charge. Finally, a high-torque servo winch is installed to control the incidence angle of the canopy to provide the proper canopy configuration for powered or gliding flight.

The cup and vane anemometer shown in Fig. 10 was placed 4 m above ground level and within 20 m horizontally of the target location to provide relevant wind data while protecting it from potential collision with an aerial system. The ground station laptop polled the anemometer for ground wind measurements at a rate of 1 Hz. These data were recorded to the computer before being transmitted to the onboard autopilot through a 2.4-GHz XBee wireless transceiver configured to communicate with the wireless transceiver mounted on the payload. A schematic of the experimental setup is presented in Fig. 14. While the anemometer was simply integrated into the preexisting base station framework, it could easily be operated by a simple microcontroller with a wireless link. Such a device would be a low-cost, lightweight, and highly portable tool for improving the landing accuracy of guided airdrop systems.

TABLE IV
LANDING STATISTICS FROM FLIGHT TEST RESULTS

Autonomous System	50% CEP	90% CEP	Reduction in 50% CEP
Nominal Autonomous	17.5 m	38.0 m	–
Anemometer Aided	12.0 m	29.3 m	33%

Testing was conducted in Eloy, Arizona on clear days with low- to medium-wind magnitudes. Significant wind direction changes were noted at various altitudes during flight testing, indicating that the conditions were well suited to test the effectiveness of the ground wind system. Furthermore, tests were conducted in northern Georgia, where more rolling terrain and forest-lined fields provide for variable wind conditions. A total of 59 flights were conducted testing the nominal autonomous system and 25 flights with the anemometer-aided system for a total of 85 experimental landings. Landing dispersion results of these tests are displayed in Fig. 15, plotted in the WF, and landing accuracy statistics are presented in Table IV.

The nominal autonomous system has a 50% CEP 17.7 m, and a 90% CEP of 38.0 m. The 50% CEP is close to simulation results by design as the Dryden turbulence level was a simulation parameter. However, the experimental 90% CEP value being smaller than the simulated value indicates that the simulation generated wind fields with greater variability, causing an increase in simulated outliers. The 50% CEP and 90% CEP for the anemometer-aided airdrop system were 12.0 and 29.3 m, respectively. These results show a 33% improvement in the median miss distance for the anemometer-aided guided airdrop system over the nominal autonomous system. Additionally, a 23% improvement was found in the 90% CEP. These improvements are theorized to stem from two sources. First, the anemometer measurement provides better estimates of the airdrop system's location in the WF. Second, with both onboard atmospheric wind estimates and ground wind measurements, the control logic can identify potential wind shears at lower altitudes. As a result, an averaged wind field is used in calculations

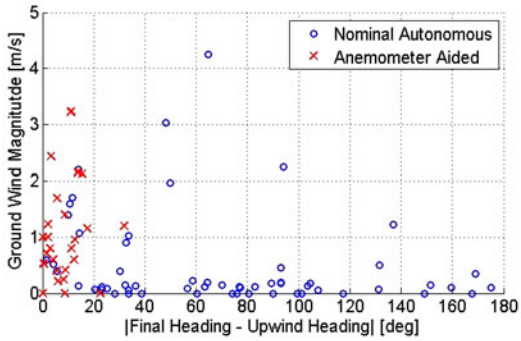

Fig. 16. Ability of the experimental-guided airdrop system under nominal and anemometer-aided conditions to land into the wind.

which helps prepare the airdrop system to enter a wind shear in a good location with respect to the landing target. This information regarding wind shears has been proven to be highly relevant as unexpected wind shears below 100 m in altitude have the potential to cause landing miss distances of over 100 m [23]. Finally, over and under shooting the target is primarily attributed to the uncertainty of spatially variable vertical wind components and the time variation of wind. A test flown primarily through atmospheric sinks can result in an overestimate of the descent rate estimate causing the system to enter final approach early and overshoot the target.

The experimental platform also showed a significantly improved ability to land into the wind as shown in Fig. 16. The experimental results show slightly more heading error in comparison to simulation results, however, the reduction in heading error when the ground wind is provided to the airdrop system is dramatic compared to the nominal results. The nominal autonomous system had an average heading error of 70.0°, while the anemometer-aided system was reduced by nearly a factor of 10 to 8.7°. With a ground-based anemometer, the improved ability to land into the wind ensures that impact energy will be reduced for softer landings and increased payload survivability.

V. Conclusion

This study examines the benefits of providing ground wind data to a guided airdrop system to enhance landing accuracy and landing survivability. Conventional guidance logic representing the current state of the art was enhanced by incorporating the onboard wind estimates with ground wind measurements, transmitted via wireless link from a cup and vane placed at the drop zone to provide an improved estimate of the wind profile. Monte Carlo simulations performed using a well-validated model of the parafoil and payload system indicate that knowledge of the ground winds alone provide 80% of the benefit in landing accuracy that would be obtained with perfect knowledge of the entire wind profile. This indicates that any efforts to provide accurate estimates of the atmospheric conditions to a guided airdrop system should focus heavily on the winds near the ground. Accurate ground wind direction measurements also significantly improved the ability of the system to land into the wind, minimizing impact velocity and maximizing payload survivability. The improvements in landing accuracy predicted in simulation were then verified with 85 experimental flight tests on a small-scale airdrop system. Aggregate landing accuracy improvements of over 30% along with a complete elimination of hazardous cross and downwind landings were demonstrated when ground data were made available to the guided airdrop system. The anemometer and transceiver system is low cost, lightweight, and highly portable, making it a feasible addition to equipment provided to ground crews awaiting cargo delivery at the drop zone. These characteristics make ground wind anemometers both highly advantageous and very straight forward to integrate into current autonomous airdrop operations.

Acknowledgment

The authors would like to thank the Natick Soldier Research Development and Engineering Center Airdrop Technology Team.

References

[1] R. Ducote and R. Speelman, "US Air Force concepts for accurate delivery of equipment and supplies," *J. Aircraft*, vol. 4, no. 4, p. 383–392, 1967.
[2] M. P. Gionfriddo, "A survey of the U.S. Army R&D programs in airdrop," presented at the 2nd Amer. Inst. Aeronautics Astronautics Aerodynamic Decelerator Syst. Technol. Conf., Houston, TX, USA, 1966.
[3] HQ USAF/XOO, Flight operations: Computed air release point procedures, Air Force Instruction 11–231, pp. 1–178, Aug. 2005.
[4] K. Kelly and B. Pena, "Wind study and GPS dropsonde applicability to airdrop testing," presented at the 16th Amer. Inst. Aeronautics Astronautics Aerodynamic Decelerator Syst. Technol. Conf., Boston, MA, USA, 2001.
[5] S. Dellicker, R. Benney, S. Patel, T. Williams, C. Hewgley, O. Yakimenko, R. Howard, and I. Kaminer, "Performance, control, and simulation of the affordable guided airdrop system," in *Proc. Amer. Inst. Aeronautics Astronautics Modeling Simul. Technol. Conf. Exhib.*, 2000, vol. 4309, pp. 14–17.
[6] M. Ward, M. Costello, and N. Slegers, "Specialized system identification for parafoil and payload systems," *J. Guidance, Control, Dynamics*, vol. 35, no. 2, pp. 588–597, 2012.
[7] M. Ward, M. Costello, and N. Slegers, "On the benefits of in-flight system identification for autonomous airdrop systems," *J. Guidance, Control, Dynamics*, vol. 33, no. 5, pp. 1313–1326, 2010.
[8] R. Wright, R. Benney, and J. McHugh, "Precision airdrop system," in *Proc. Amer. Inst. Aeronautics Astronautics Aerodynamic Decelerator Syst. Conf.*, 2005, vol. 1644, pp. 23–26.
[9] T. A. Herrmann, M. B. Ward, M. Costello, and N. Slegers, "Utilizing ground-based LIDAR for autonomous airdrop," in *Proc. 2nd Amer. Inst. Aeronautics Astronautics Aerodynamic Decelerator Syst. Technol. Conf.*, 2013, pp. 1288–1300.
[10] I. Antoniou, M. Courtney, H. E. Jørgensen, T. Mikkelsen, S. Von Hunerbein, S. Bradley, B. Piper, M. Harris, I. Marti, M. Aristu, D. Foussekis, and M. P. Nielsen, "Remote sensing the wind using Lidars and Sodars," presented at the Eur. Wind Energy Conf. Exhib., Milan, Italy, 2007.
[11] T. F. Goodrick and A. Murphy, "Analysis of various automatic homing techniques for gliding airdrop systems with comparative performance in adverse winds," presented at the Amer. Inst. Aeronautics Astronautics, Aerodynamic Deceleration Syst. Conf., Palm Springs, CA, USA, 1973.
[12] T. Jann, "Advanced features for autonomous parafoil guidance, navigation and control," presented at the 18th Amer. Inst. Aeronautics Astronautics Aerodynamic Decelerator Syst. Technol. Conf. Seminar, Munich, Germany, 2005.
[13] I. I. Kaminer and O. A. Yakimenko, "Development of control algorithm for the autonomous gliding delivery system," presented at the Amer. Inst. Aeronautics Astronautics Aerodynamic Decelerator Syst. Technol. Conf. Seminar, Monterey, CA, USA.
[14] E. Ewing, H. Bixby, and T. Knacke, "Recovery systems design guide," Defense Tech. Inf. Center, Fort Belvoir, VA, USA, Tech. Rep. AFFDL-TR-78-151, 1978.
[15] T. Gimadieva, "Optimal control of a gliding parachute system," *J. Math. Sci.*, vol. 103, no. 1, pp. 54–60, 2001.

[16] H. Tennekes, "The logarithmic wind profile," *J. Atmospheric Sci.*, vol. 30, no. 2, pp. 234–238, 1973.
[17] A. Clauset, C. R. Shalizi, and M. E. Newman, "Power-law distributions in empirical data," *SIAM Review*, vol. 51, no. 4, pp. 661–703, 2009.
[18] L. E. Dubins, "On curves of minimal length with a constraint on average curvature, and with prescribed initial and terminal positions and tangents," *Amer. J. Math.*, vol. 79, pp. 497–516, 1957.
[19] M. Ward, "Adaptive glide slope control for parafoil and payload aircraft," Ph.D. dissertation, Dept. Aerospace Eng., Georgia Inst. Technol., Atlanta, GA, USA, p. 138, 2012.
[20] R. E. Kalman, "A new approach to linear filtering and prediction problems," *J. Basic Eng.*, vol. 82, no. 1, pp. 35–45, 1960.
[21] *Flying Qualities of Piloted Aircraft*, MIL-STD-1797A, 1990.
[22] N. Slegers, E. Beyer, and M. Costello, "Use of variable incidence angle for glide slope control of autonomous parafoils," *J. Guidance, Control, Dynamics*, vol. 31, no. 3, pp. 585–596, 2008.
[23] O. A. Yakimenko, N. J. Slegers, and R. A. Tiaden, "Development and testing of the miniature aerial delivery system snowflake," presented at the 20th American Inst. Aeronautics Astronautics Aerodynamic Decelerator Syst. Technol. Conf., Seattle, WA, USA, 2009.

Martin R. Cacan received the Bachelor of Science degree from the University of California, Berkeley, CA, USA, in 2011, and the Master of Science degree from the Georgia Institute of Technology (Georgia Tech), Atlanta, GA, USA, in 2013, both in mechanical engineering.

He is currently a Graduate Research Assistant at Georgia Tech conducting research in dynamic modeling and advanced control methodologies for autonomous airdrop systems.

Edward Scheuermann received the B.S. degree in mechanical engineering from Louisiana State University, Baton Rouge, LA, USA, in 2009, and the M.S. degree in mechanical engineering from Georgia Tech, Atlanta, GA, USA, in 2012.

He is currently a Graduate Research Assistant in the Center for Advanced Machine Mobility, Georgia Tech. His research includes dynamic modeling, simulation, and control of aerospace vehicles with a focus on airdrop system technologies.

Michael Ward received the Bachelor's degree in mechanical and aerospace engineering from the University of California, Irvine, CA, USA, in 2006, and the Ph.D. degree from Georgia Tech, Atlanta, GA, USA, in May 2012, for work on guidance, navigation, and control development for autonomous airdrop systems.

He is currently a Postdoctoral Researcher at Georgia Tech for Mark Costello specializing in the field of aircraft flight dynamics and autonomous control.

Mark Costello received the B.S. degree in aerospace engineering from Pennsylvania State University, University Park, PA, USA, in 1987, and the M.S. and Ph.D. degrees in aerospace engineering from the Georgia Institute of Technology, Atlanta, GA, USA, in 1989 and 1992, respectively.

He is currently a Professor in the Guggenheim School of Aerospace Engineering and the Woodruff School of Mechanical Engineering, Georgia Institute of Technology. He is the Director of Center for Advanced Machine Mobility, a multidisciplinary research center consisting of a network of faculty and students focused on mobile platform technologies. He works in the area of dynamics, control, and design.

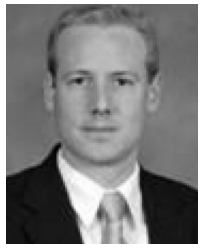

Nathan Slegers received first B.S. degree in applied science from George Fox University, Newberg, OR, USA, in 1999, and second in mechanical engineering from the University of Washington, Seattle, WA, USA, in 2000. He received the M.S. and Ph.D. degrees in mechanical engineering from Oregon State University, Corvallis, OR, USA, in 2002 and 2004, respectively.

He is currently an Associate Professor in the College of Engineering at George Fox University, Newburg, Oregon, USA. His research focuses on the intersection of dynamic modeling, control engineering, and robotics to optimize performance.